Large-Scale Surface Responses during European Dry Spells Diagnosed from Land Surface Temperature

SONJA S. FOLWELL

Centre for Ecology and Hydrology, Crowmarsh Gifford, Wallingford, United Kingdom

PHIL P. HARRIS AND CHRISTOPHER M. TAYLOR

Centre for Ecology and Hydrology, Crowmarsh Gifford, and National Centre for Earth Observation, Wallingford, United Kingdom

(Manuscript received 22 April 2015, in final form 31 July 2015)

ABSTRACT

Soil moisture plays a fundamental role in regulating the summertime surface energy balance across Europe. Understanding the spatial and temporal behavior in soil moisture and its control on evapotranspiration (ET) is critically important and influences heat wave events. Global climate models (GCMs) exhibit a broad range of land responses to soil moisture in regions that lie between wet and dry soil regimes. In situ observations of soil moisture and evaporation are limited in space, and given the spatial heterogeneity of the landscape, are unrepresentative of the GCM gridbox scale. On the other hand, satelliteborne observations of land surface temperature (LST) can provide important information at the larger scale. As a key component of the surface energy balance, LST is used to provide an indirect measure of surface drying across the landscape. To isolate soil moisture constraints on evaporation, time series of clear-sky LST are analyzed during dry spells lasting at least 10 days from March to October. Averaged over thousands of dry spell events across Europe, and accounting for atmospheric temperature variations, regional surface warming of between 0.5 and 0.8 K is observed over the first 10 days of a dry spell. Land surface temperatures are found to be sensitive to antecedent rainfall; stronger dry spell warming rates are observed following relatively wet months, indicative of soil moisture memory effects on the monthly time scale. Furthermore, clear differences in surface warming rate are found between cropland and forest, consistent with contrasting hydrological and aerodynamic properties.

1. Introduction

Soil moisture plays a fundamental role in controlling the surface energy budget through its constraint on evapotranspiration (ET). In regions of high soil moisture seasonality, such as the European midlatitudes, soil moisture deficits develop during spring and summer. This shifts the surface energy budget toward greater sensible heat production as latent heat flux is reduced, which warms and dries the overlying air. This in turn can establish feedbacks on soil moisture through increased evaporative demand and impacts on cloud cover and precipitation. Several authors have linked historic summer heat wave and drought events in Europe to summer soil moisture state (Chiriaco et al. 2014; Weisheimer et al. 2011) and more specifically to precursor spring soil moisture deficits (Bisselink et al. 2011; Fischer et al. 2007b). Miralles et al. (2014) showed that under certain conditions soil moisture–induced atmospheric heating can persist above the nocturnal boundary layer and accumulate over several days to produce mega-heat waves. They attribute the strength of the 2003 European and 2010 Russian heat wave events to this mechanism. Similarly, nonlocal effects may play a role, with anomalously low winter and spring soil moisture patterns propagating northward from the Mediterranean to central and northern Europe, through transportation of warm dry air (Quesada et al. 2012; Vautard et al. 2007b; Zampieri et al. 2009). Established soil moisture deficits can then interact with the large-scale circulation to amplify the summertime temperature variability (Fischer et al. 2007a). These feedbacks can lead to increased air temperatures and drought

Corresponding author address: Sonja S. Folwell, Centre for Ecology and Hydrology, CEH Wallingford, Benson Lane, Crowmarsh Gifford, Wallingford OX10 8BB, United Kingdom.
E-mail: ssf@ceh.ac.uk

DOI: 10.1175/JHM-D-15-0064.1

conditions over wide areas through cloud suppression; increased shortwave radiation; reduced precipitation; and the import of warmer, drier air masses. Land cover also plays an important role, particularly in a well-watered regime, with forests contributing higher sensible heat fluxes than grasslands during heat waves in response to developing daytime vapor pressure deficits (Stap et al. 2014). Beyond the meteorological domain, summer heat wave events, such as in 2003, have important effects on human health (Garcia-Herrera et al. 2010), air quality (Vautard et al. 2007a), and the regional carbon cycle (Ciais et al. 2005).

Capturing these land–atmosphere feedbacks in global climate models (GCMs) is problematic. Analysis of GCM simulations in phase 3 of the Coupled Model Intercomparison Project (CMIP3) shows wide disagreement in the extent to which soil moisture availability constrains summer evapotranspiration in central and eastern Europe (Boé and Terray 2008). This feature is also present in a more recent group of regional climate models run under the ENSEMBLES project (Boé and Terray 2014), and a multimodel analysis of regional climate simulations under the European branch of the Coordinated Regional Climate Downscaling Experiment (EURO-CORDEX) showed a large spread in the strength and duration of European heat waves (Vautard et al. 2013). The simulation of soil moisture dynamics is a key factor in the warm temperature bias in future climate predictions (Christensen and Boberg 2012). A key limitation in improving GCM behavior is the poor availability of widespread observations of soil moisture and evaporation. Where in situ observations of evaporation exist, they can provide useful characterization of evaporative behavior at the scale of individual flux tower footprints. Teuling et al. (2006) and Blyth et al. (2010) show that total evaporation during drydowns declines exponentially as the water store is depleted, with *e*-folding times of 15–35 days in regions of high soil moisture variability and longer where seasonal droughts are more common. Teuling et al. (2006) also show a stronger variation of time scale with land cover than with soil texture.

In principle, satellite remote sensing datasets provide the opportunity to observe the impact of soil moisture deficits on the land surface at spatial scales simulated by global and regional climate models. Remotely sensed products have been used to generate hybrid datasets such as Global Land Surface Evaporation: The Amsterdam Methodology (GLEAM; Miralles et al. 2011), a modeled daily global evaporation product principally using remotely sensed net radiation, precipitation, and soil moisture; and FLUXNET–Multi-Tree Ensemble (MTE; Jung et al. 2011), which uses a machine learning technique to extrapolate from the flux site scale to a global 0.5° × 0.5° grid of surface fluxes. However, in a comparison of ET from multiple satellite-based datasets with purely modeled ET estimates, Mueller et al. (2011) conclude that the large uncertainties within the observational datasets prevent evaluation of climate model biases.

The particular focus of this study is on the use of remotely sensed land surface temperature (LST). Global datasets of LST and normalized difference vegetation index (NDVI), related to vegetation leaf area, have been routinely retrieved under cloud-free conditions for many years. They provide indications of the surface energy budget and vegetation response to water stress, respectively, for example, the 2003 heat wave over Europe (Teuling et al. 2010; Zaitchik et al. 2006). The LST is sensitive to physical properties of the surface such as surface roughness; albedo; and crucially, soil moisture as well as local meteorology. Over vegetated surfaces LST responds to soil moisture deficits in the root zone via reductions in stomatal conductance, whereas for nonvegetated or partially vegetated surfaces, LST responds to near-surface soil moisture that controls the evaporation rate direct from the soil surface.

A number of techniques have been developed to compute evapotranspiration from LST [see Kalma et al. (2008) for a review of methods], exploiting its relatively high spatial resolution, primarily to provide estimates of evaporation for hydrological modeling and water resource assessments. The methods vary in complexity, with the more complex surface energy balance methods using LST to diagnose the sensible heat flux, computing ET as a residual term, for example, Surface Energy Balance Algorithm for Land (SEBAL; Bastiaanssen et al. 1998) and Atmosphere–Land Exchange Inverse (ALEXI; Anderson et al. 2007; Norman et al. 1995), which employs a two-source energy balance scheme separating bare soil evaporation and transpiration. Computing sensible heat fluxes requires accurate estimates of the surface roughness and/or aerodynamic temperature and necessitates complex algorithms and detailed observations of land cover as well as local meteorology. Less complex are the triangle (Carlson 2007) and latterly trapezoidal methods that exploit relationships between LST, vegetation indices (VIs), and soil moisture. These methods require a degree of calibration, based upon a single scene containing wet and dry pixels in order to constrain the temperature ranges. Often detailed surface energy balance models or empirical relationships are prerequisites for deriving evapotranspiration, as is extrapolation from instantaneous to hourly, daily, or monthly estimates of ET. An important limitation in estimating ET from LST is the availability of cloud-free scenes, though methods

for gap filling have been developed (Anderson et al. 2008). At the same time, data assimilation schemes have been developed for land surface models, enabling adjustments to a state variable or parameter directly in order to reduce the difference between the observed and modeled surface temperature (e.g., Castelli et al. 1999). An alternative approach assimilates an LST-based soil moisture proxy into a soil–vegetation–atmosphere transfer model and shows potential in improving soil moisture estimates over direct assimilation of LST (Crow et al. 2008). While these methods of estimating surface fluxes from LST implicitly capture the soil moisture control on LST, the relationships between soil moisture and LST remain difficult to quantify, particularly over scales relevant for GCMs.

In this study, rather than determine evapotranspiration from LST, we develop a methodology to analyze the impacts of soil water stress on the surface energy balance at the large scale using time series of LST. Focusing on temporal anomalies in LST reduces the sensitivity of the results to uncertain parameters such as aerodynamic roughness lengths. In this paper we adopt an approach similar to that used by Teuling et al. (2006), where the focus is on observations within a rain-free period. However in place of flux site measurements of evaporation, we examine the evolution of remotely sensed LST over Europe during dry spells of 10 days or longer. In section 2, we develop a simple model to illustrate the behavior of land surface temperature during an idealized dry spell. Descriptions of the observational datasets and methods are provided in sections 3 and 4. Details of dry spell evolution of LST and the sensitivity of the LST signal to land cover and antecedent rainfall are presented in section 5. Finally, the vegetation response and broader discussion of the results are presented in section 6, followed by conclusions in section 7.

2. A simple model of LST evolution under rain-free conditions

To illustrate the influence of a drying surface on LST, we first present a simple model representing the energy and water balance at the land surface. These two systems interact at the surface via evaporation E (bare soil evaporation and transpiration). In the absence of rain and assuming drainage and runoff to be negligible, the water balance is simplified so that evaporation losses lead directly to a reduction in soil moisture s with time t:

$$\frac{ds}{dt} = -E. \tag{1}$$

The energy balance at the land surface is expressed in terms of fluxes per unit area ($\mathrm{W\,m^{-2}}$):

$$R_n = H + \lambda E + G, \tag{2}$$

where R_n is net downward radiation balanced by sensible heat H, latent heat λE, and soil heat G fluxes. Sensible and latent heat fluxes are expressed as

$$H = \frac{\rho_a c_p}{r_a}(T_s - T_a) \tag{3}$$

and

$$\lambda E = \frac{\rho_a}{r_a + r_s}[q_{\mathrm{sat}}(T_s) - q_a], \tag{4}$$

where ρ_a is the density of moist air ($\mathrm{kg\,m^{-3}}$), c_p is the heat capacity of air ($\mathrm{J\,kg^{-1}\,K^{-1}}$), T_s is surface temperature or LST (K), T_a is air temperature (K), r_a is aerodynamic resistance ($\mathrm{s\,m^{-1}}$), λ is latent heat of vaporization of water ($\mathrm{J\,kg^{-1}}$), q_{sat} is saturated specific humidity ($\mathrm{kg\,kg^{-1}}$), q_a is specific humidity ($\mathrm{kg\,kg^{-1}}$), and r_s is surface resistance ($\mathrm{s\,m^{-1}}$). Net radiation is determined from downwelling shortwave and longwave radiation (S_d and L_d, respectively), surface albedo α, and longwave emission from the surface:

$$R_n = S_d(1 - \alpha) + L_d - \varepsilon\sigma T_s^4, \tag{5}$$

where surface emissivity is ε and σ is the Stefan–Boltzmann constant.

Following (Monteith 1965), linearization of $q_{\mathrm{sat}}(T_s)$ and longwave emission $\varepsilon\sigma T_s^4$ in terms of air temperature, and substituting Eqs. (3)–(5) into Eq. (2), yields an expression for surface temperature:

$$T_s = \frac{\left\{S_n + L_d - G + 3\varepsilon\sigma T_a^4 + \dfrac{\rho_a c_p}{r_a} T_a - \dfrac{\lambda\rho_a}{r_a + r_s}[q_{\mathrm{sat}}(T_a) - \Delta(T_a)T_a - q_a]\right\}}{4\varepsilon\sigma T_a^3 + \dfrac{\lambda\rho_a}{r_a + r_s}\Delta(T_a) + \dfrac{\rho_a c_p}{r_a}}, \tag{6}$$

where $\Delta(T_a)$ is the slope of the temperature–vapor saturation curve at T_a and S_n is net shortwave radiation. This relationship allows the influence of the resistance terms to be considered independently for a constant

forcing. Soil moisture acts on latent heat flux through r_s. Here we assume a linear reduction in r_s when soil moisture (i.e., s), expressed in terms of water depth (mm), falls below a critical soil moisture threshold s_c:

$$r_s = \begin{cases} r_s^{\min}, & s > s_c \\ r_s^{\min}\left(\frac{s_c}{s}\right), & s \le s_c \end{cases}. \quad (7)$$

We simulate instantaneous midmorning LST over a homogeneous surface during a rain-free period. Assuming that under rain-free conditions water in the soil is held under capillary pressure and that interception and drainage are negligible, then Eq. (1) will apply and moisture for evaporation is entirely met by water available in the soil column. Thus, for each subsequent day the soil moisture declines by an amount equal to the daily evaporation and, on each new day, the updated soil moisture is used to compute r_s according to Eq. (7) and instantaneous LST using Eq. (6). The midmorning evapotranspiration rate is rescaled to provide a daily total using instantaneous and daily total incoming shortwave radiation. The LST is simulated for 50 days assuming constant values of net shortwave radiation (440 W m^{-2}), downwelling longwave radiation (330 W m^{-2}), air temperature (290 K), specific humidity (7.8 g kg^{-1}), and emissivity (0.95). In this simple model, a constant ground heat flux of 10 W m^{-2} is assumed for the dry spell duration.

The outputs from this idealized model are used to illustrate the evolution of LST during a simulated dry spell and are further used to explore the LST sensitivity to surface properties. First, we consider a single simulation (Figs. 1a,c,e; solid dark line) performed with an initial soil moisture 5 mm above the critical point (s_c = 30 mm) and aerodynamic and surface resistance values (r_a = 50 s m^{-1}; $r_s^{\min}$ = 80 s m^{-1}) typical of short crop cover. It is first useful to consider soil moisture and evaporation rates (Figs. 1a,c; solid dark line) in the context of stages of evaporative behavior (e.g., Salvucci 1997; Teuling et al. 2010). On days 1–4, soil moisture is above the critical point and evaporation rates are constant, characteristic of a well-watered surface (stage 1 drying). After day 4, soil moisture levels fall below the critical point, and the evaporation rate declines, that is, the surface is in a water-limited regime (stage 2 drying). It takes 24 days of stage 2 drying for ET to drop to 1/e of its stage 1 value. This compares with observed values of between 18 and 21 days at a grassland site in northern Europe (Teuling et al. 2006). In the plot showing LST with time (Fig. 1f; solid dark line) we see a similar but inverted pattern to the ET, with LST constant at 295 K during the stage 1 regime, and increasing when evaporation becomes water limited (stage 2). Once ET is negligible, also referred to as stage 3 (Teuling et al. 2010), the LST will remain at a higher value, in this case 302 K. The LST warming amplitude can be a useful way to characterize the aerodynamic response of the surface when we have dry spells long enough to capture the full drydown. In reality, over much of northern and central Europe we are rarely able to observe a complete drydown, so rather than consider the LST amplitude between wet and dry states, we consider the warming over the first 10 days of the dry spell. In the first example of crop cover, we have an average 10-day warming rate of 0.075 K day^{-1}.

We now consider the impact of aerodynamic resistance, a term that influences how efficiently the turbulent energy transfer occurs from the surface to the atmosphere. In Figs. 1a, 1c, and 1e, the dashed and dotted lines represent simulations with a low (r_a = 20 s m^{-1}) and high (r_a = 100 s m^{-1}) aerodynamic resistance, typical values under moderate winds for forest or crop-covered surfaces, respectively. In both cases, modest differences in soil moisture have developed after 20 days, in response to accumulated ET differences. All three cases show similar stage 1 and stage 2 behavior and drydown e-folding times ranging between 23 and 24 days. However, the notable effect is on the absolute values of LST on day 1: 293 and 300 K for aerodynamic resistances of 20 and 100 s m^{-1}, respectively. The average 10-day warming rate for low and high r_a is 0.043 and 0.085 K day^{-1}, respectively, that is, when r_a is low we have efficient turbulent mixing reducing LST in absolute terms and in its range. In the same set of plots, the solid gray line (Figs. 1a,c,e) illustrates the LST response for the same aerodynamic resistance as the first case, that is, 50 s m^{-1}, but for a surface with a shallow soil moisture reservoir (15 instead of 30 mm) and soil moisture critical point of 15 mm, typical for bare soil. Again the soil moisture is initialized with a value 5 mm above this threshold. Here the LST amplitude is the same as in the first case; however, the notable difference is in the reduced duration of the stage 2 regime, equivalent in this case to an e-folding time of 15 days. After 25 days, the reservoir is effectively empty and no further changes occur.

A second important factor influencing dry spell LST evolution is initial soil moisture at the onset of the dry spell. In Figs. 1b, 1d, and 1f, we show three simulations assuming three increasingly dry initial soil moisture s_{ini} states (35, 20, and 5 mm). In the first case (solid dark line) the initial soil moisture is above the critical point, and the initially constant LST leads to a low average 10-day warming rate. In contrast, in the second case (dash–dotted line) the initial soil moisture is below the critical point, evaporation is constrained at the onset of the dry spell, and the 10-day warming rate is high at 0.15 K day^{-1}.

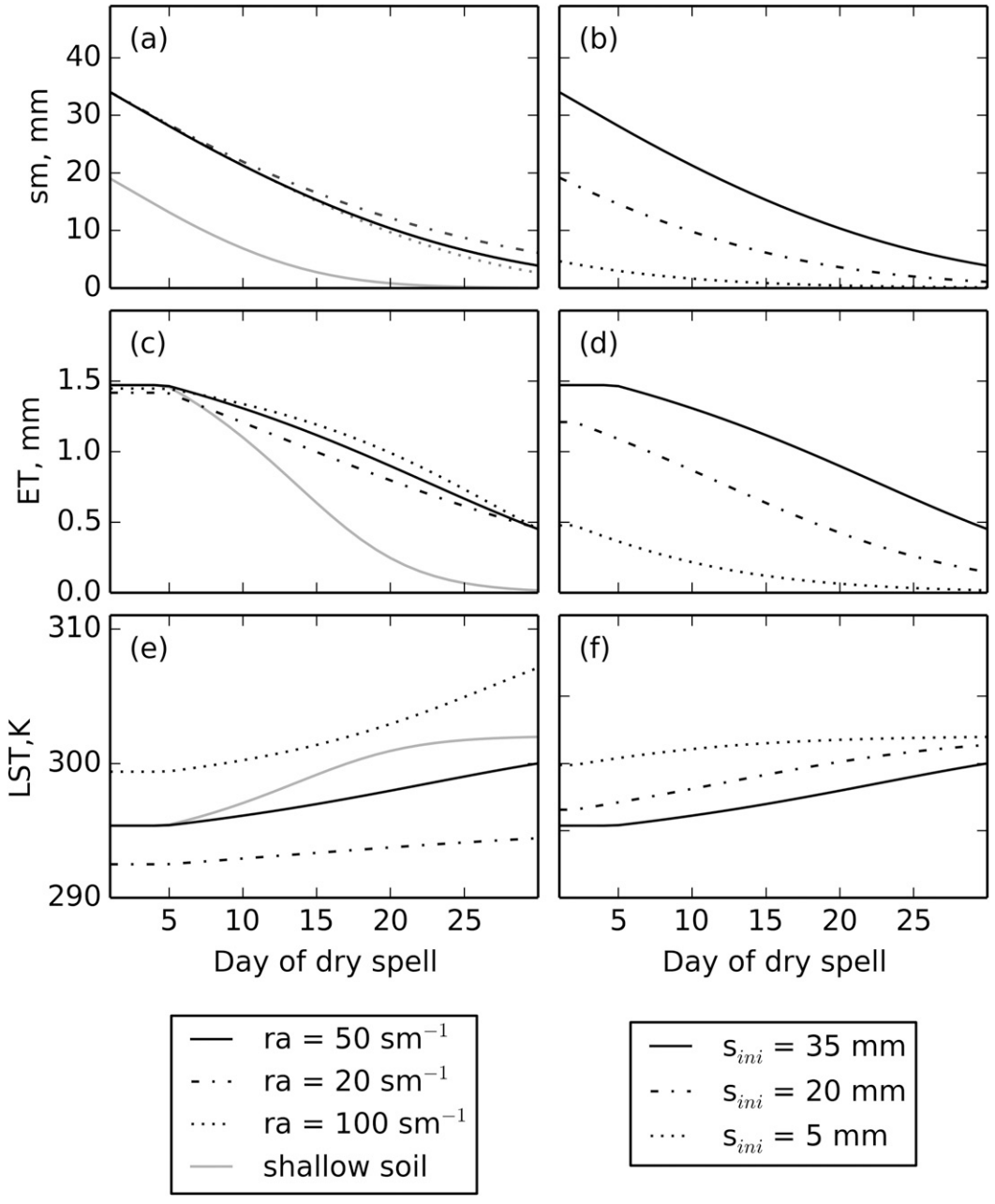

FIG. 1. (a),(b) Simulated s (mm); (c),(d) daily ET (mm); and (e),(f) instantaneous LST (K) during a dry spell comparing (left) the influence of r_a of 20, 50, and 100 s m^{-1} and soil reservoir size and (right) increasingly dry s_{ini} of 35, 20, and 5 mm.

Finally, in the third case (dotted line), initial soil moisture levels are approaching zero, evaporation is severely limited, and moving from stage 2 drying to negligible moisture availability, resulting in a weaker 10-day warming rate of 0.12 K day^{-1}.

The relationship between the 10-day warming rate and initial soil moisture is summarized in Fig. 2a, using the same example of crop cover (boldface line with plus signs). The surface warming rate exhibits some nonlinear behavior with respect to initial soil moisture. Purely stage 1 drying (warming rate of 0) is evident for initial soil moisture values well above the critical point. Between 42 and 31 mm, the dry spell includes both stage 1 and stage 2 drying. For decreasing values of initial soil moisture (down to about 12 mm) the surface is experiencing stage 2 drying, and warming rates rise as LST

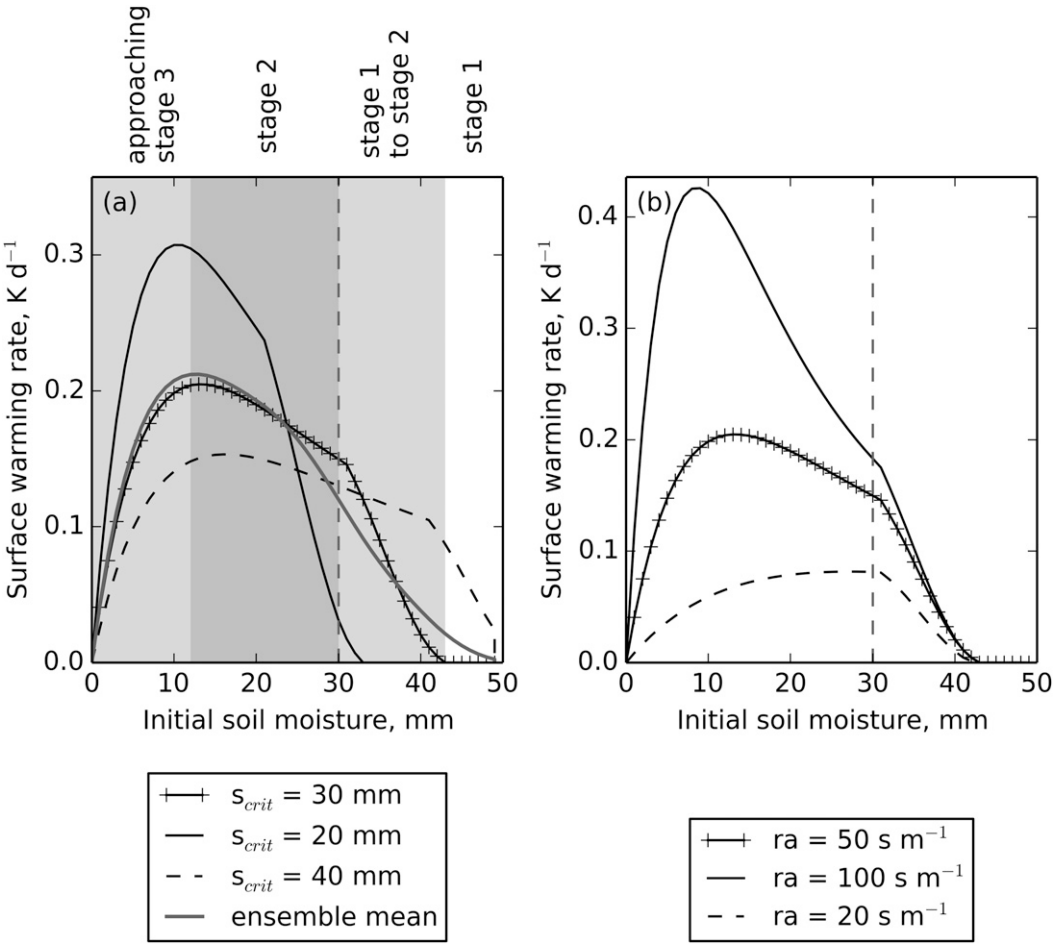

FIG. 2. Average surface warming rates obtained from linear regressions fitted to the first 10 days of simulated LST, plotted against s_{ini} for three cases of (a) soil moisture critical points and (b) r_a. Plus signs denote values obtained for a single simulation. The shaded areas indicate the dominant drying phase as related to a soil of s_c = 30 mm (vertical dashed line).

sensitivity to soil moisture increases. Finally, for initial values of 10 mm or less, approaching stage 3, the surface dries out more slowly, which reduces the dry spell surface warming rate. In Fig. 2a, the effect of differing soil critical points is also compared. Shallower soil reservoirs show higher average warming rates overall as 10 days of accumulated evapotranspiration depletes a larger fraction of the reservoir. Within a single satellite pixel, we expect to sample surfaces with a range of soil moisture capacities. The gray curve illustrates the integrated response of a surface with critical points ranging between 20 and 40 mm. This ensemble response produces a smoothed curve relative to the three specific cases. However, the soil moisture value at which the maximum gradients occur is relatively unchanged in all cases. Figure 2b illustrates the sensitivity of surface warming rates to aerodynamic resistance, using the same low (20 s m^{-1}) and high (100 s m^{-1}) aerodynamic resistances shown in Fig. 1. As expected, the higher aerodynamic resistances have larger warming rates for a given soil moisture initialization. This sensitivity to aerodynamic resistance decreases for wetter soils.

This model illustrates the evolution of LST for a fixed set of atmospheric conditions and a simple description of the surface. In practice, our satellite-derived observations contain surfaces with a range of initial soil moisture states, vegetation and soil properties sampled under a variety of atmospheric conditions, reservoir sizes, and aerodynamic resistances.

3. Datasets

a. *Earth observation datasets*

This study makes extensive use of Earth observation datasets acquired from spaceborne sensors, primarily

LST, fraction of absorbed photosynthetically active radiation (fPAR) to provide a measure of vegetation dynamics, and a land-cover dataset. We use clear-sky LST derived from the Moderate Resolution Imaging Spectroradiometer (MODIS) on board the *Terra* polar-orbiting satellite, available since 2000. The *Terra* satellite makes an overpass at approximately 1100 local time each day, sensing thermal infrared (TIR) through two channels. The LST product is derived via the generalized split window algorithm (Wan 2008). The level 3 LST product (MOD11A1, collection 5) is available at a 1-km resolution on the MODIS sinusoidal grid and is only used here when accompanied by the highest-data-quality flag (pixel-level quality assurance = 0), equivalent to average LST errors $\leq$1 K. In addition, to reduce the known effect of biases at high view angles, pixels where the satellite view angle exceeds 55° are rejected. The 1-km sinusoidal data are aggregated to a regular 0.5° grid by averaging across all available 1-km pixels for each grid box. A significant challenge for using LST time series to monitor land surface behavior is the availability of cloud-free observations, particularly over more northerly latitudes in Europe. This can introduce errors due to subgrid sampling variability within a single 0.5° grid box from day to day. To minimize this effect, before aggregating data to 0.5°, we compute LST anomalies at the 1-km scale, where daily data are compared to a long-term climatology. The climatological values for each 1-km pixel are generated in two steps: 1) all available data (2000–12) within a particular month are averaged and 2) the climatological value for each day of the year is computed from linear interpolation between adjacent monthly means. It is the resulting anomalies that are averaged up to the 0.5° grid. Clearly, a more robust estimate of the 0.5° LST anomaly is obtained when the grid box contains a high number of pixels. Therefore, associated with each daily aggregated LST anomaly are the numbers of 1-km pixels contributing to the gridbox mean. Finally, a grid box with fewer than 100 pixels on any day is rejected from the analysis.

In addition to 0.5° mean observations, we also calculate LST anomalies derived only from crop or forest pixels, based on the static MODIS land-cover-type product (MCD12Q1) at 500-m resolution. The IGBP classification is employed to attribute each 1-km LST pixel to a dominant land-cover type. A crop pixel at 1 km is defined using the cropland and cropland/natural mosaic IGBP classes, while forest includes evergreen needleleaf, evergreen broadleaf, deciduous needleleaf, deciduous broadleaf, and mixed forest classes. The LST 1-km data are attributed to a land-cover type prior to the aggregating step so that anomalies for each contributing land-cover type can be computed separately for each 0.5° grid box.

The MODIS fPAR product MCD15A3, also at 1-km resolution, is based on reflectance data in the 400–700-nm spectral range—the wavelengths important for photosynthesis—and provides a measure of the greenness of the land surface. Information from both the MODIS *Terra* and *Aqua* platforms are combined over a 4-day window and are only available from July 2002. Values of fPAR range between 0 and 1, with a value of 1 indicating all of the available radiation (PAR) within the band is absorbed. As for LST, the daily 1-km fPAR climatologies are computed. The 1-km data are aggregated to 0.5° resolution, identifying all pixels within the 0.5° grid box and taking the average over all available pixels and calculating the anomaly at 0.5°.

b. *Meteorological datasets*

Meteorological datasets are required for two purposes: 1) to identify periods when there is no rainfall and 2) to provide air temperature at the mean time of the satellite overpass. The Water and Global Change (WATCH) Forcing Data–ERA-Interim (WFDEI; Weedon et al. 2014) is a 0.5°-resolution global meteorological product providing a consistent set of meteorological variables at a 3-hourly time step. It is derived from the ECMWF interim reanalysis (ERA-Interim; Dee et al. 2011), which ingests satellite, atmospheric sounding, and surface observations. The ERA-Interim data are interpolated to a 0.5° $\times$ 0.5° grid prior to bias corrections being applied. Air temperature and precipitation fields are bias corrected against gridded observations of monthly air temperature, monthly precipitation, and number of rain days per month taken from CRU Time Series, version 3.0 (CRU TS3.0; prior to 2010) and CRU Time Series, version 3.1 (CRU TS3.1; 2010–12). The WFDEI 2-m air temperatures are derived from the reanalysis 10-m air temperature with elevation adjustments made using an environmental lapse rate. Monthly total rain days are only corrected where the interpolated ERA-Interim totals are more than 2 days above the observations, which is predominantly in the tropics, while underestimates are left unchanged, maintaining consistency over multigrid frontal precipitation as well as across temperature, humidity, and shortwave fields. Monthly precipitation totals are adjusted to match the observations. ERA-Interim contains seasonal corrections of aerosol loading, important over northern Europe; however, additional interannual correction of aerosol loading on downward shortwave radiation is also applied, again by comparing against CRU TS3.0 and CRU TS3.1 cloud cover. For our analysis of LST the WFDEI precipitation has been aggregated to provide daily precipitation from 0000 to 2400 UTC, and other 3-hourly

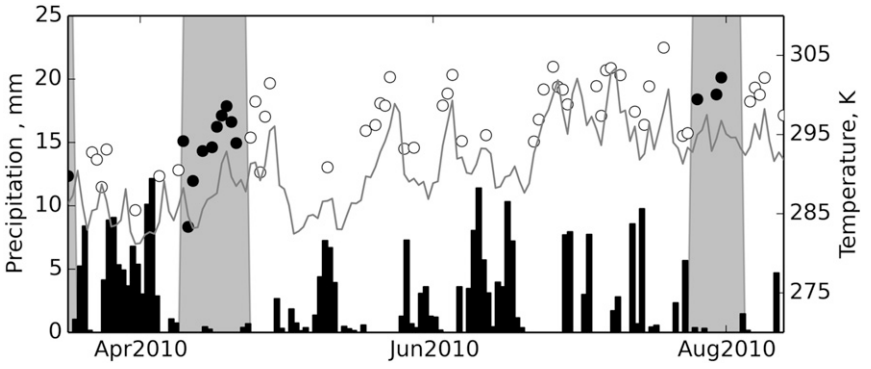

FIG. 3. Illustration of dry spells in the gridded daily WFDEI precipitation time series for a grid box in northern France. Dry spells (gray shading) are defined as periods of at least 10 days during which there is no more than 0.5 mm day^{-1} of precipitation. When precipitation exceeds this threshold, the dry spell event is terminated. Observed LST (circles) and T_a (gray line) are at 1030 local time. Filled circles indicate LST observations that occur during a dry spell.

WFDEI values were interpolated linearly to the approximate local overpass time.

Observations of gauged precipitation records in the independently compiled E-OBS, version 9 (Haylock et al. 2008), provide an alternative source of observed daily precipitation for Europe that is used to evaluate daily WFDEI precipitation. The period of analysis covers the warm season (March–October) for the years 2000–12, that is, the period over which both MODIS *Terra* LST observations and WFDEI data are available.

4. Method

a. LST during dry spell events

Analysis of the LST time series is confined to rain-free periods, during which we expect the surface to be drying. These rain-free periods, or dry spells, are identified from the WFDEI daily precipitation time series, providing a catalog of dry spell events against which LST anomalies are retrieved. A dry spell event is defined as a period of 10 days or more having no more than 0.5 mm of precipitation per day. It is implicit in this definition that a minimum of 0.5 mm of precipitation falls during the 24 h preceding each dry spell. This is illustrated for a single grid box in northern France for 2010 (Fig. 3). It is clear that this definition yields relatively few dry spells per year from which to sample LST. The strict event termination rule means that we may truncate longer dry spells, thus omitting useful LST observations from our analysis, but it enables a clearer interpretation of the results. Overall, the number of dry spells in more northerly latitudes is limited and the choice of minimum dry spell length of 10 days reflects the trade-off between identifying long enough dry spells and maintaining a sufficient quantity of observations.

A second point to note from Fig. 3 is the strong correlation between air temperature and LST. While LST can drive air temperatures, in midlatitudes it is particularly important to account for the impact that daily variations in air temperatures have on LST, for example, from advection. Crucially, it is the difference between the surface and air temperature, rather than LST itself that provides a more direct indication of soil moisture state. Therefore, in our analysis we derive a diagnostic comparing the 0.5° LST anomalies to the 0.5° WFDEI air temperature anomalies. We compute air temperature anomalies at the corresponding MODIS overpass time, and a composite of the difference in clear-sky temperature anomalies (TD) is built up over many events and locations. This TD diagnostic is calculated for each dry spell day across all events as follows:

$$\mathrm{TD}_j = \frac{\sum_{i=1}^{n} w_{ij}[(T_{s,ij} - T^c_{s,ij}) - (T_{a,ij} - T^c_{a,ij})]}{\sum_{i=1}^{n} w_{ij}}, \qquad (8)$$

where j is the dry spell day, n is the total number of dry spell events, and i is a single event with a valid LST observation and corresponding air temperature. The variables T^c_s and T^c_a are the climatological land surface and air temperatures, respectively, and w is the number of cloud-free 1-km pixels used to construct a particular 0.5° LST value. Values of gridded air temperature are only selected on days with a valid 0.5° LST value, so T^c_s and T^c_a both represent clear-sky temperature climatologies. A simpler alternative metric, based on absolute rather than anomalous surface temperature data

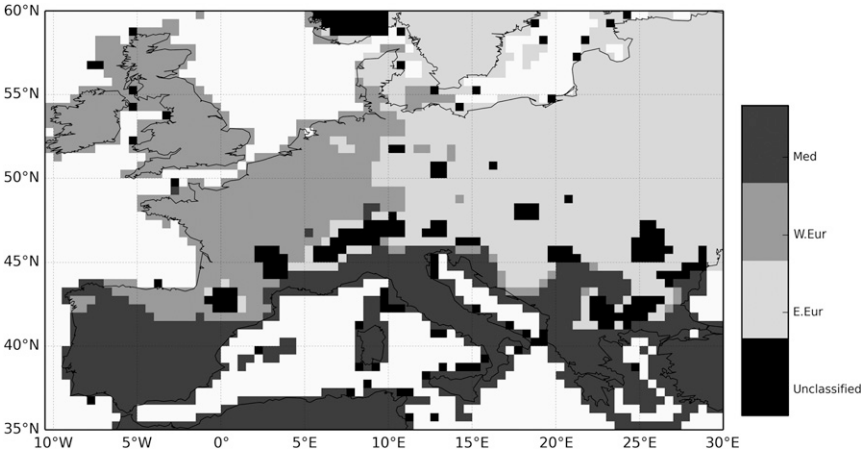

FIG. 4. The European domain used in the analysis, including regional groupings of 0.5° grid cells (black indicates areas that are unclassified and excluded from the groupings).

(i.e., $T_s - T_a$), is of course possible. However, as noted in the previous section, that approach would increase errors associated with spatial sampling of the heterogeneous surface on days with partial cloud cover. Dry spell events are identified for each grid box during March–October of the period 2000–12, though cases where the air temperature falls below 278 K are removed to limit the influence of frozen soils at high latitudes and altitudes in our analysis.

b. *Domain and grouping*

The areal extent of analysis over Europe is shown in Fig. 4. The domain covers the region (35.25°–60.25°N, 10.25°W–28.25°E), which extends into northern Africa and Russia, comprises 2839 land points on the WFDEI grid, and produces 112 034 dry spell events during our study period. This window encompasses the range of summertime evaporation constraints, that is, radiation-limited in the north and soil moisture–limited in the south, that have been described in other studies (e.g., Teuling et al. 2009). To examine the influence of climate—specifically, the effect of seasonal variations in evaporation and precipitation on soil moisture and LST evolution—grid boxes are grouped by climate zone. Three broad regions are identified based upon the Köppen–Geiger climate classifications of Peel et al. (2007): western Europe (Cfb), eastern Europe (Dfb), and the Mediterranean and Iberia (BSk, BSh, BWh, BWk, Csa, Csb, Cfa, Dsb). A number of mountainous/alpine grid boxes are unclassified and not included in the analysis.

The Mediterranean and Iberia region has a strongly seasonal climate characterized by cool, wet winters and hot, dry summers (Fig. 5a). Annual precipitation (2000–12) of 720 mm is the lowest of the three regions and peaks in December. Using the strict definition of a dry spell, the Mediterranean region averages five dry spells per grid box over 838 grid boxes per warm season (March–October), with a peak in June (Fig. 5a). Incident solar radiation is high throughout the spring and summer, with evaporation rates highest in spring and becoming water limited throughout the summer months. Western Europe has a maritime climate, with an average annual precipitation (2000–12) of 1030 mm and relatively constant precipitation throughout the year. The seasonal cycle in soil moisture is driven primarily by evapotranspiration, which is in turn controlled by radiation and soil water availability. The total number of dry spells exhibits a weak annual peak in March and produces typically only three dry spell events per grid box per warm season over 693 grid boxes. The eastern European region has drier, colder winters than western Europe and lower annual precipitation (760 mm; 2000–12), with peak rainfall in July. Dry spells occur most frequently in March and October with an average of three dry spells per grid box (over 1094 grid boxes) per warm season, although a small number of events in March may include periods where the ground is frozen. High levels of insolation and water availability due to high summer precipitation lead to high rates of evaporation. Figures 5b, 5d, and 5f illustrate the number of dry spell days per year in each region, showing some interannual variation in the western and eastern European regions, though much less in the Mediterranean where the warm months have a relatively low frequency of rain days with little year-to-year variation. In western Europe a peak in the number of dry spell days is observed in the year 2003, a significant year in terms of drought and extreme temperatures and reflecting the wide spatial scale of the event. In eastern Europe, the

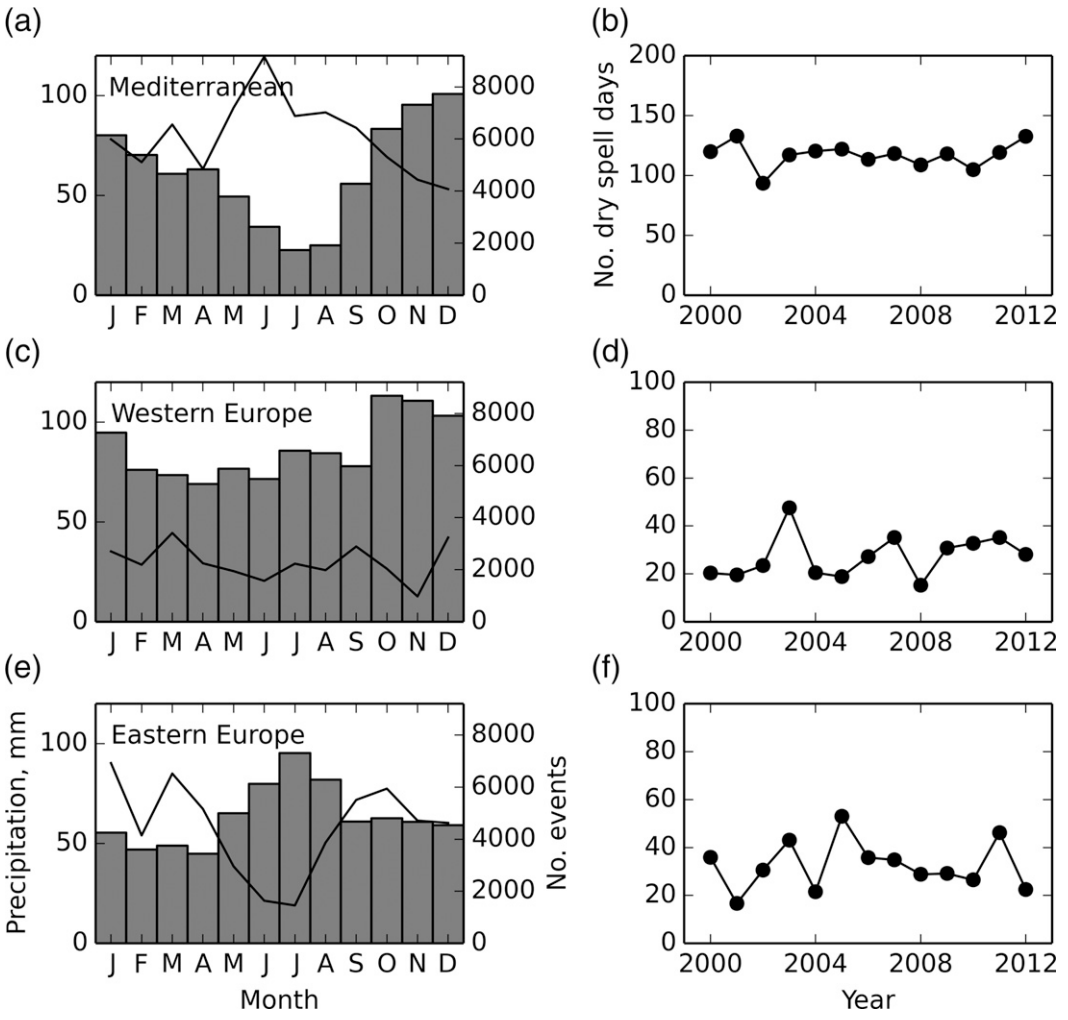

FIG. 5. (a),(c),(e) Mean monthly precipitation (bars) derived from WFDEI precipitation (years 2000–12) and number of dry spell events starting in that month (lines) including cases below the min temperature threshold; (b),(d),(f) the average number of warm season (March–October) dry spell days per grid box per year.

years 2005 and 2011 have high numbers of dry spell days; in both cases these are concentrated in late summer (August–October).

5. Evolution of LST and TD during dry spells

Considering the three regions described above, we now examine how LST and the TD diagnostic evolve during dry spells. Within each region, there are at least 10 000 distinct observations of LST anomalies at the 0.5°-scale per day during the first 10 days of the dry spell (indicated by bar plots in Figs. 6a–c). In all three regions, there is typically an increase in the number of observations over the first 3 days. There is also a corresponding increase in composite mean surface pressure (not shown), consistent with an increased frequency of anticyclonic conditions and a reduction in cloud cover across large areas. The number of clear-sky observations remains approximately constant on days 4–10, before declining because of fewer long-lived dry spells in the dataset. In particular, for eastern and western Europe, the number of observations falls away quickly after 10 days, making any interpretation of the composite beyond 12 days prone to sampling biases. For example within western Europe, while the contribution to the composite of a relatively dry subregion such as southwestern France is approximately constant during the first 10 days, it becomes more dominant by day 15 because of the higher frequency of long dry spells there, compared to, for example, the British Isles.

The composite LST and gridded air temperature on clear-sky days and their respective climatologies are plotted in Figs. 6a–c. For each region, the composite air temperature (gray solid line) is initially lower than the

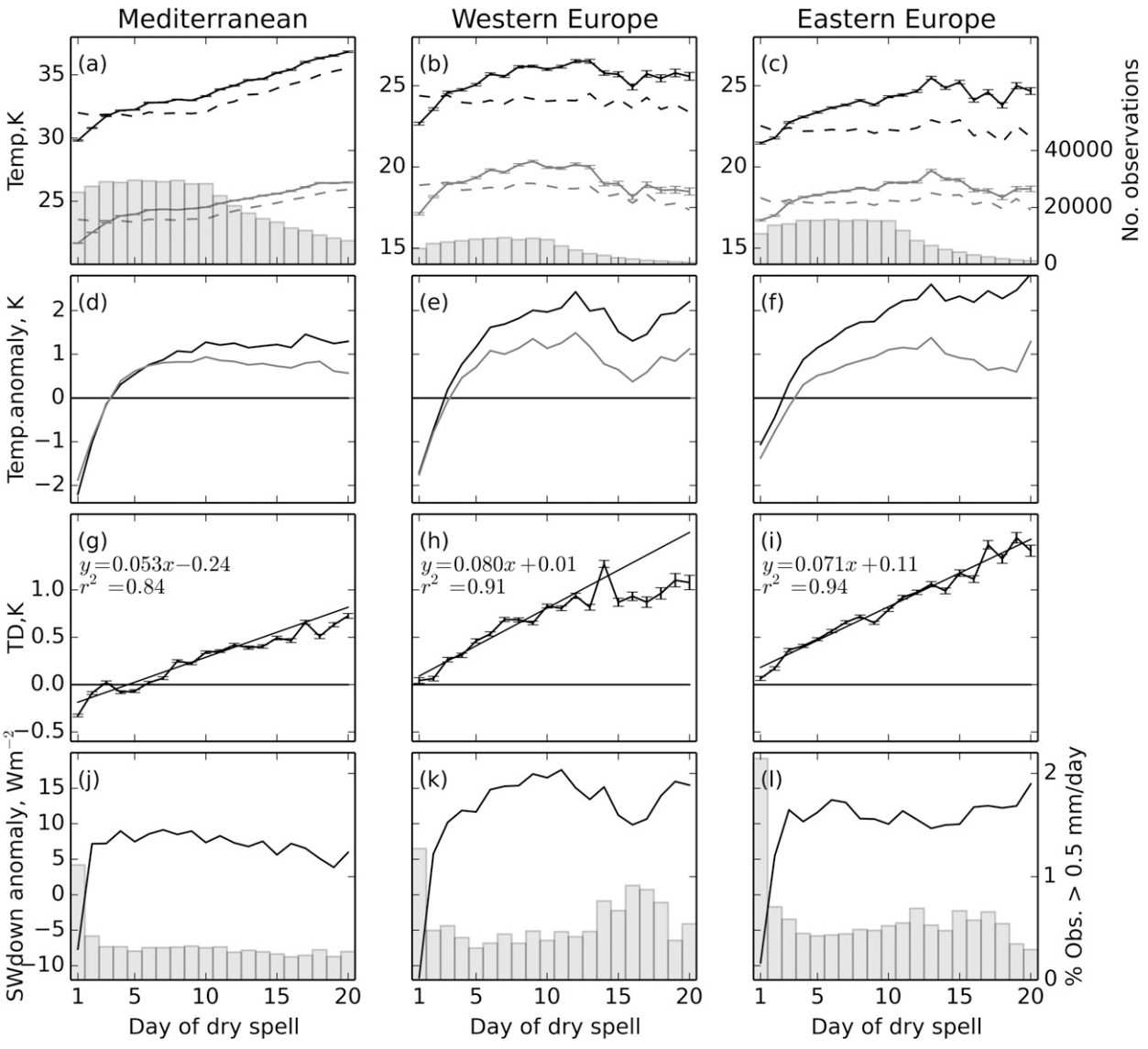

FIG. 6. Composites of temperature during dry spells for three regions showing (a)–(c) LST (black, solid) and T_a (gray, solid) and associated climatologies (dashed), where bars represent the number of 0.5° grid cells contributing to each value; (d)–(f) composite LST anomalies (black) and T_a anomalies (gray); (g)–(i) TD as it evolves during a dry spell; and (j)–(l) composite downward shortwave radiation (line), where bars indicate the percentage of observations in which precipitation is greater than 0.5 mm in the European Climate Assessment & Dataset (ECA&D) record of observed precipitation. Linear regressions are fitted against days 2–11. Error bars indicate standard errors on the mean.

corresponding clear-sky air temperature climatology (gray dotted line) but exceeds it after 3–4 days. Likewise, the composite LST (black solid line) is initially lower than the LST climatology (black dashed line) crossing over after 2–3 days. The LST and air temperature anomalies are more easily compared in Figs. 6d–f. Each region displays a consistent signal of increasingly positive surface and air temperature anomalies as the number of days since rainfall increases. In eastern and western Europe, after about 12 days the relatively low number of observations starts to introduce noise to the composite temperature signal. Figures 6g–i show the difference between surface and air temperature anomalies TD, capturing the relative warming at the surface compared to the overlying atmosphere. The error bars are computed as the standard error on the mean. To enable a quantitative comparison of the curves, we fit linear regressions, using ordinary least squares, to the daily mean values of TD over days 2–11. Day 1 is omitted because of the possible influences of low

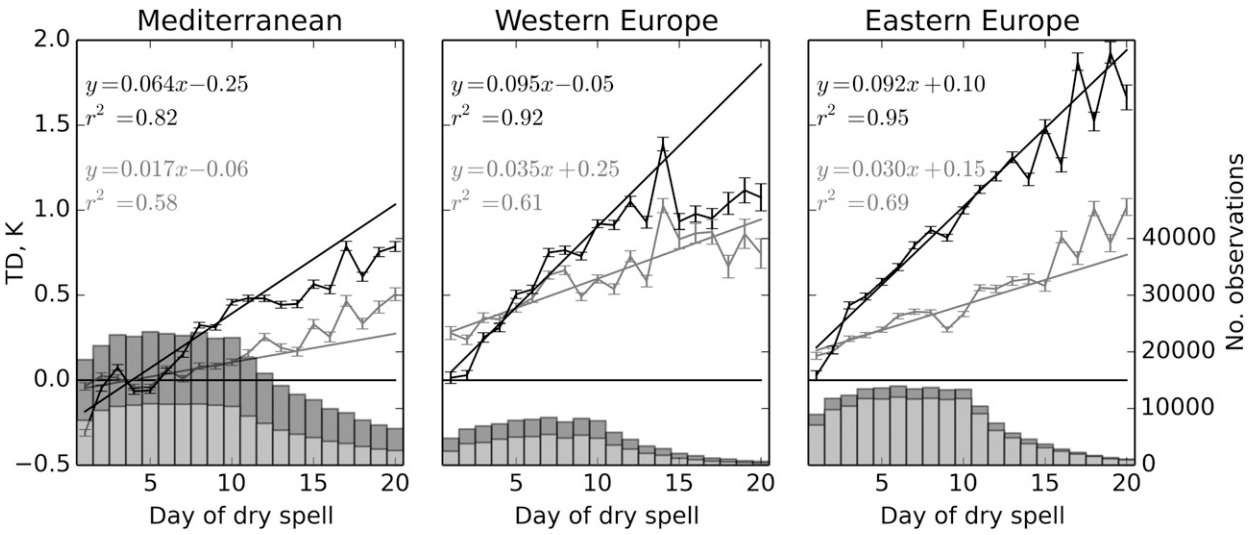

FIG. 7. Composite TD (K) over forest (gray) and over grassland and crop cover (black) for eastern Europe. Unstacked bars indicate number of LST values contributing to each day. Linear regressions are fitted against days 2–11. Error bars indicate standard errors on the mean.

numbers of observations and WFDEI precipitation errors (Figs. 6j–l). The TD increases are strongly linear with a high coefficient of determination r^2 (>0.84) for the fitted regressions in the three regions during the window of 2–11 days. The standard error provides an estimation of the random errors (such as sensor noise), and it is substantially reduced by averaging across large numbers of observations (i.e., $N \sim 10^4$), hence the small error bars around each TD value. However, other systematic errors are apparent, such as the sawtoothed pattern seen from day 13 onward in Fig. 6i, and that is due to a combination of the MODIS repeat time being about 2 days, so that different sets of dry spells are sampled on alternate days, and the low number of observations contributing to the mean TD. Bearing in mind that a single dry spell lasting several days may coexist across many 0.5° grid boxes, at a low number of observations this effect can become apparent, particularly over a smaller number of events (e.g., Fig. 7).

The negative anomalies observed on days 1 and 2 in the Mediterranean are indicative of the impact of rain preceding the dry spell in a relatively dry climate. This diagnostic, although not a direct measure of sensible heat flux, provides an estimate of variations in clear-sky sensible heat. Using Eq. (3) and assuming values of $r_a = 50\,\mathrm{s\,m^{-1}}$, typical for crop cover under intermediate wind speed, a TD of +1 K is equivalent to an additional $20\,\mathrm{W\,m^{-2}}$ in sensible heat at the overpass time, corresponding to 10%–20% of typical sensible heat fluxes, depending on surface conditions.

An important factor for LST is incoming shortwave radiation. To check whether the dry spell TD composite could be influenced by variations in cloud cover (either directly via errors in the MODIS cloud mask, or indirectly via reduced insolation in the minutes and hours preceding the overpass), we present the composite downward shortwave radiation anomalies from WFDEI (Figs. 6j–l, black lines), again sampled only at a corresponding MODIS clear-sky overpass. The composites exhibit notable negative insolation anomalies on day 1 in all three regions, consistent with relatively large cloud cover at the 0.5° scale on the morning after rain, an effect that may suppress observed clear-sky LST. For the remainder of the composite, insolation remains fairly constant in the Mediterranean and eastern Europe, indicating that the observed rise in LST is not due to an increase in insolation, but a response to the drying surface. However, in western Europe the continued increase in insolation (about $10\,\mathrm{W\,m^{-2}}$ over 10 days) may also contribute to the warming signal in this region. An important caveat here is that while WFDEI shortwave radiation is independent of the MODIS satellite data, it is a model product, albeit one that well captures synoptic variations in cloud cover in Europe (Weedon et al. 2014).

Finally, to assess the quality of WFDEI in identifying rain-free periods, we present the frequency of rain days (totals exceeding 1 mm) based on the independent E-OBS gauge dataset (Figs. 6j–l; bars, right-hand axis). After day 1, the frequency of recorded rain days within the dry spell composites is considerably less than 1% for all three regions. Bearing in mind that in WFDEI gauge data are only used to correct ERA-Interim precipitation at the monthly time scale, we conclude that WFDEI

(and the underlying ERA-Interim) does a remarkably good job in depicting European dry spells.

It is instructive to compare the observed TD diagnostic with the simulations of LST from the idealized model (Fig. 1). The observed regional composites all show fairly consistent day-on-day increases in LST relative to air temperature over the 20 days analyzed in Fig. 6. When compared to the idealized model, this implies some degree of moisture limitation on ET in the observations right from the onset of the dry spell. The observed warming rates are lower than those simulated by the simple model using an intermediate value of aerodynamic resistance (Fig. 2b) for most values of initial soil moisture. However, the simulated warming rate is rather sensitive to the prescribed surface properties, the relationship between soil moisture and ET, and the atmospheric forcing. Moreover, those simulations do not consider complex combinations of covarying surface properties or the buffering effect of groundwater and irrigation, which are likely to affect the observed signal. In the next sections, we focus on how the observed warming rates vary with land cover and initial soil moisture.

a. Sensitivity to land cover

The idealized model illustrates that, during dry spells, we expect lower surface warming rates over forest than over short vegetation purely from aerodynamic effects (Fig. 2b). We also expect weaker and delayed surface warming when the soil reservoir is larger (Fig. 2a), for example, because of the well-established deep roots of forests, compared to annual grasses or crops. Using LST anomalies from only forest or crop pixels at the 1-km scale, the composite TD is plotted in Fig. 7 for three regions. Note that the land-cover classifications used are fixed in time and no account is made for seasonal changes in vegetation cover within each class. We see from Fig. 7 that TD increases with day into the dry spell for both forest and crop classes, and that TD on day 2 is consistently lower over crops than forests. As before, linear regressions are fitted to TD over days 2–11. The 95% confidence intervals are provided for the warming rates. The warming rate over this period is consistently higher over crop cover (0.06 ± 0.02, 0.1 ± 0.02, and $0.09 \pm 0.02\,\mathrm{K\,day^{-1}}$) than forest ($0.02 \pm 0.01$, 0.04 ± 0.02, and $0.03 \pm 0.015\,\mathrm{K\,day^{-1}}$) in the Mediterranean, western Europe, and eastern Europe, respectively. The observed ratios of warming rate over crop cover compared with forest for each region are 3.8, 2.7, and 3.1 for Mediterranean, western Europe, and eastern Europe, respectively. These ratios can be compared with outputs from the idealized model to explore the expected impact of aerodynamic effects only. In Fig. 2b, the ratio of warming rates for a smooth (intermediate) surface with $r_a = 100\,\mathrm{s\,m^{-1}}$ ($50\,\mathrm{s\,m^{-1}}$) relative to a rough surface with $r_a = 20\,\mathrm{s\,m^{-1}}$, varies from 2.9 (2.1) when initialized at the critical soil moisture to 7.3 (3.4) when warming rates are maximized with respect to initial soil moisture. This comparison indicates that aerodynamic effects contribute significantly to the differences between forest and crop warming rates. The composites in Fig. 7 are likely contaminated by other land-cover types because of 1) use of dominant land-cover type at 500-m resolution rather than 100% land-cover type, 2) georegistering of MODIS imagery (Tan et al. 2012), and 3) errors in the underlying land classification. When we recomputed the composites based only on pixels without land-cover boundaries, crop warming rates increased by ~10% in all regions, while forest warming rates decreased by 23% in eastern Europe and 60% in the Mediterranean. Note that restricting our analysis to pure forest areas in the Mediterranean left us with only 1100 events.

b. Sensitivity to antecedent precipitation

In the idealized model, warming rates show a strong dependence on the initial soil moisture content (Fig. 2). We now explore this sensitivity using the TD diagnostic. As extensive observations of soil moisture are not available, we use the WFDEI precipitation records to derive antecedent precipitation for 30 days prior to the onset of the dry spell. This information is used to stratify the catalog of dry spell events into deciles of antecedent precipitation. Considering the whole domain and LST over all land-cover types, the composite TD is plotted for each decile of antecedent precipitation, moving from the driest (Fig. 8; decile 1) through to the wettest decile (Fig. 8; decile 10). In the driest to moderately dry cases (deciles 1–4) and in the wettest case (decile 10), the linear regression presents a relatively poor approximation, with $r^2 < 0.8$. In deciles 7–9, a strongly linear relationship emerges, with values of $r^2 > 0.9$ and TD gradients from 0.07 ± 0.01 to $0.08 \pm 0.02\,\mathrm{K\,day^{-1}}$. The strongest relationship is seen in decile 8 ($r^2 = 0.97$), in which antecedent rainfall in 30 days was between 68 and 83 mm (2.3–2.8 mm $\mathrm{day^{-1}}$).

In Fig. 9, the linear regressions are summarized by plotting gradients and intercepts with deciles of antecedent precipitation. In addition, we show the results for LST derived from the cropland- and forest-only pixels. Considering all land types first (triangles), and with the exception of decile 1, the regression intercepts show a consistent decline going from dry ($+0.6 \pm 0.02$ K; decile 2) to wet (-1.0 ± 0.02 K; decile 10). The clear negative trend in intercept values is physically consistent with the impact of cumulative rain in the previous month on ET via soil moisture; that is, the wettest deciles have more

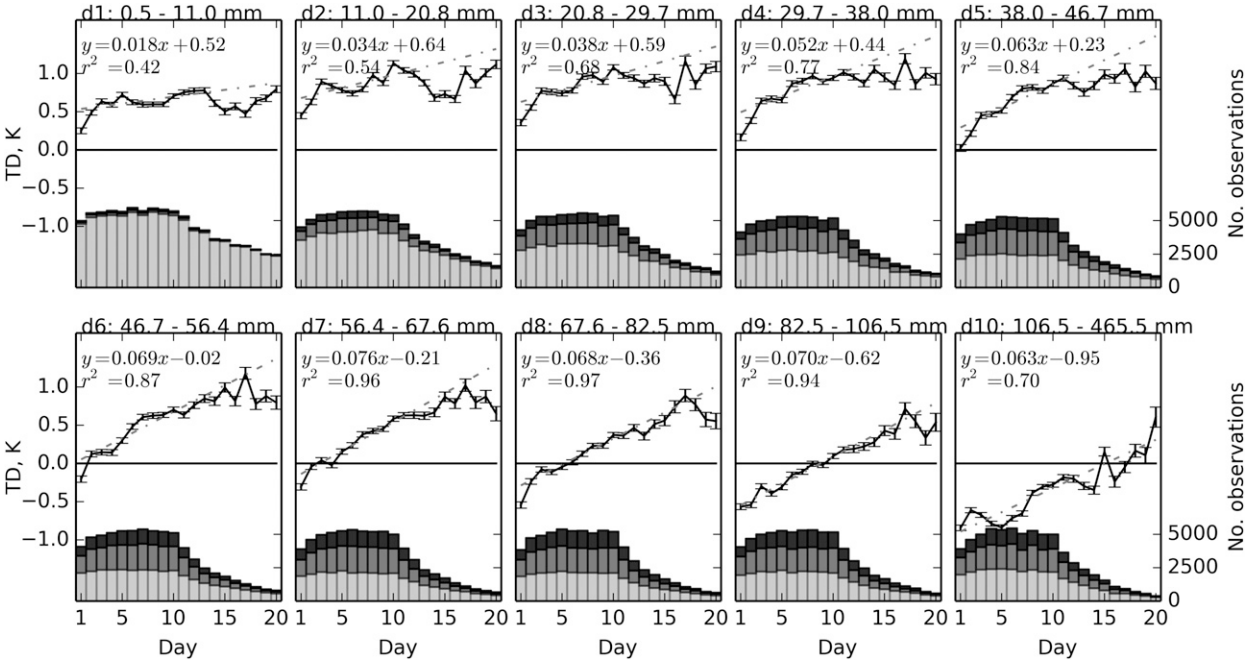

FIG. 8. Composite TD (K) anomalies for each decile of antecedent (30 day) precipitation. Linear regressions are fitted to TD on days 2–11 (dashed line). Stacked bars show the number of observations and indicate the contributions from the three climate zones: Mediterranean (light gray), western Europe (gray), and eastern Europe (dark gray). Error bars indicate standard errors on the mean.

negative initial LST anomalies and more positive ET anomalies compared to their respective climatologies.

Now considering the rate at which the land warms relative to the atmosphere during the dry spell, we see that the gradients of the regressions increase from $0.02 \pm 0.01\,\mathrm{K\,day^{-1}}$ (decile 1) to $0.08 \pm 0.02\,\mathrm{K\,day^{-1}}$ (decile 7), before falling back slightly in the final (wettest) 30% of cases. This behavior can be interpreted using the idealized model shown in Fig. 2. In the model, maximum 10-day surface warming rates occur when the initial soil moisture is well below the critical point, but not so low that the accumulated dry spell ET nearly empties the soil reservoir. Dry spell surface warming rates approach zero when initial soil moisture levels are either close to zero, or well above the critical point. Observations from different soil moisture regimes will populate different parts of this expected bell curve, and where these points lie on the curve tell us about the dominant evaporative regime there. In our case, the maximum warming rate occurs for the seventh decile of antecedent rainfall, indicating that for 60% of our events, LST is starting to plateau by the end of the dry spell, as soil moisture

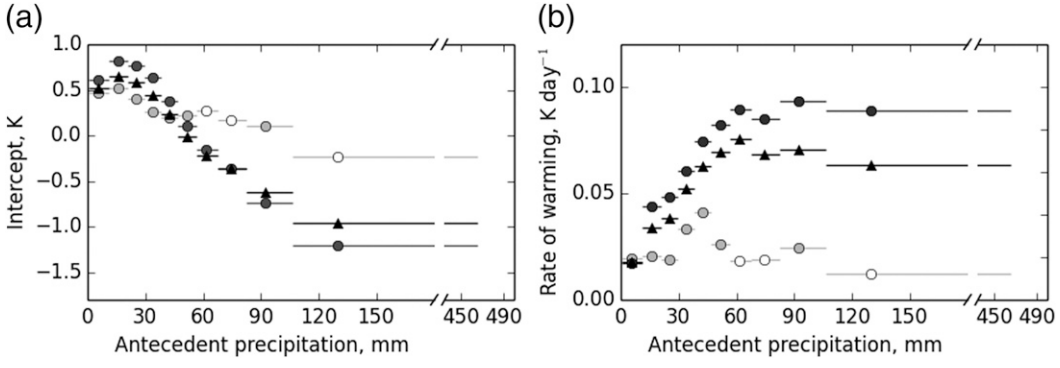

FIG. 9. Coefficients of the fitted regressions showing (a) intercepts and (b) gradients as a function of median antecedent precipitation for the whole domain for all land-cover types (triangles), crop and grassland (dark gray circles), and forests (light gray circles). The horizontal lines illustrate the antecedent precipitation ranges of each decile bin. Solid symbols are those with p values <0.05, two-tailed test; open symbols are p values ≥ 0.05.

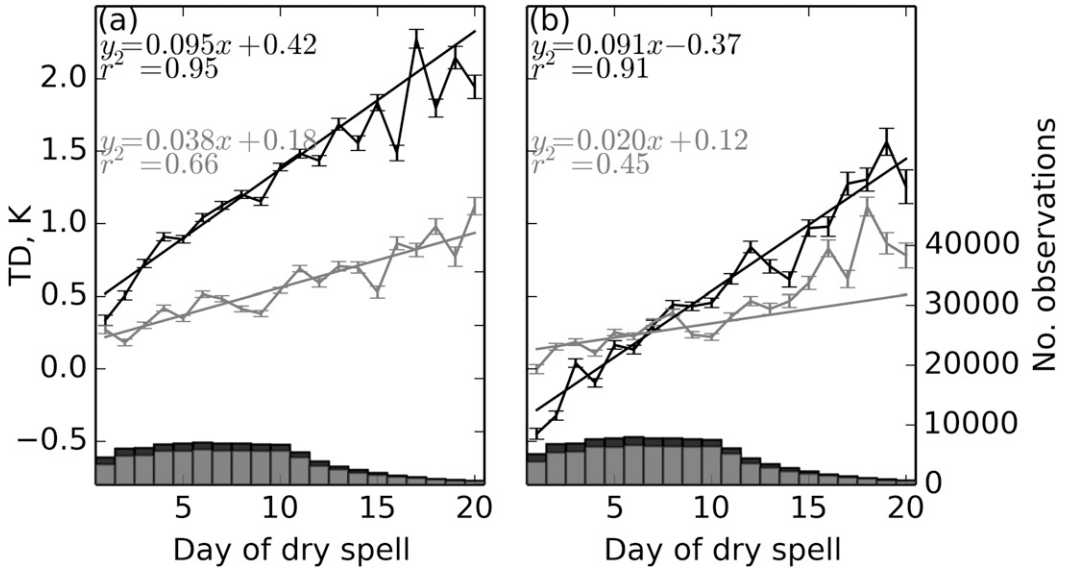

FIG. 10. Comparison of TD for the (a) dry and (b) wet halves of the dry spell event catalog comparing crop (black) and forest (gray) across eastern Europe. Unstacked bars indicate number of LST values contributing to each day crop (dark gray), forest (gray). Error bars indicate standard errors on the mean.

approaches its lower limit. Even in the wettest 30% of events, there is substantial warming (>0.05 K day^{-1}), consistent with stage 2 drying. Only within decile 10 is there any indication of purely stage 1 (i.e., unstressed) behavior, as suggested by reasonably constant TD values in the first 5 days (Fig. 8). It is important to remember that these composites represent large areas, within which there will be a broader range of local evaporative behavior.

As with the regionwide composites (Fig. 7), Europe-wide forest warming rates are substantially reduced (0.02 ± 0.02 and 0.02 ± 0.01 K day^{-1}; deciles 2 and 9, respectively) compared to crop pixels (0.04 ± 0.025 and 0.09 ± 0.02 K day^{-1}) for all but the driest decile in Fig. 9b. Interestingly, the observed ratio of crop to forest warming rate increases with soil wetness, in contrast to a predicted decrease in the simple model when considering only aerodynamic effects (Fig. 2b). In principle, this could be related to systematic sampling biases across Europe. For example, forest-classified pixels likely contain a larger bare soil component in the Mediterranean region than in northern Europe, and the Mediterranean contributes disproportionately to the driest deciles in Fig. 9. In that case, it is difficult to compare Europe-wide forest warming rates across rainfall deciles. To minimize this effect, crop and forest composites have been recomputed based only on the smaller, eastern European region, and values of TD are shown in Fig. 10 for the lower and upper halves of antecedent rainfall. As with the Europe-wide data, the ratio of crop to forest warming rates increases substantially from the driest half (2.5; Fig. 10a) to the wettest half (4.5; Fig. 10b). This behavior is inconsistent with a purely aerodynamic effect; the idealized model (Fig. 2b) predicts a decrease in the warming rate ratio for aerodynamic resistances of 50 and 20 s m^{-1} approximately from 2 to 3 (dry) down to 1.5 to 2 (wet), depending on the details of the wet and dry initialization. The likely physical interpretation of this result is that on top of the aerodynamic effect, we are detecting differences in hydrological dry spell behavior between crops and forests. In the wetter samples (Fig. 10b), forest pixels are more frequently in the stage 1 regime than crop pixels. Put another way, the forests have a larger soil moisture buffer zone than the crops, consistent with their deeper roots, and as observed in the field (e.g., Teuling et al. 2006).

6. Discussion

The composite TD provides a large-scale, aggregate surface temperature response to land drying not observed before. The sensitivity of TD to the surface physical properties (e.g., surface roughness) and its strong reliance on how wet the surface is provide confirmation that TD captures the response of the surface energy balance to water availability. This observed surface temperature response as the surface dries is driven by the ongoing transport of moisture to the atmosphere via bare soil evaporation and transpiration,

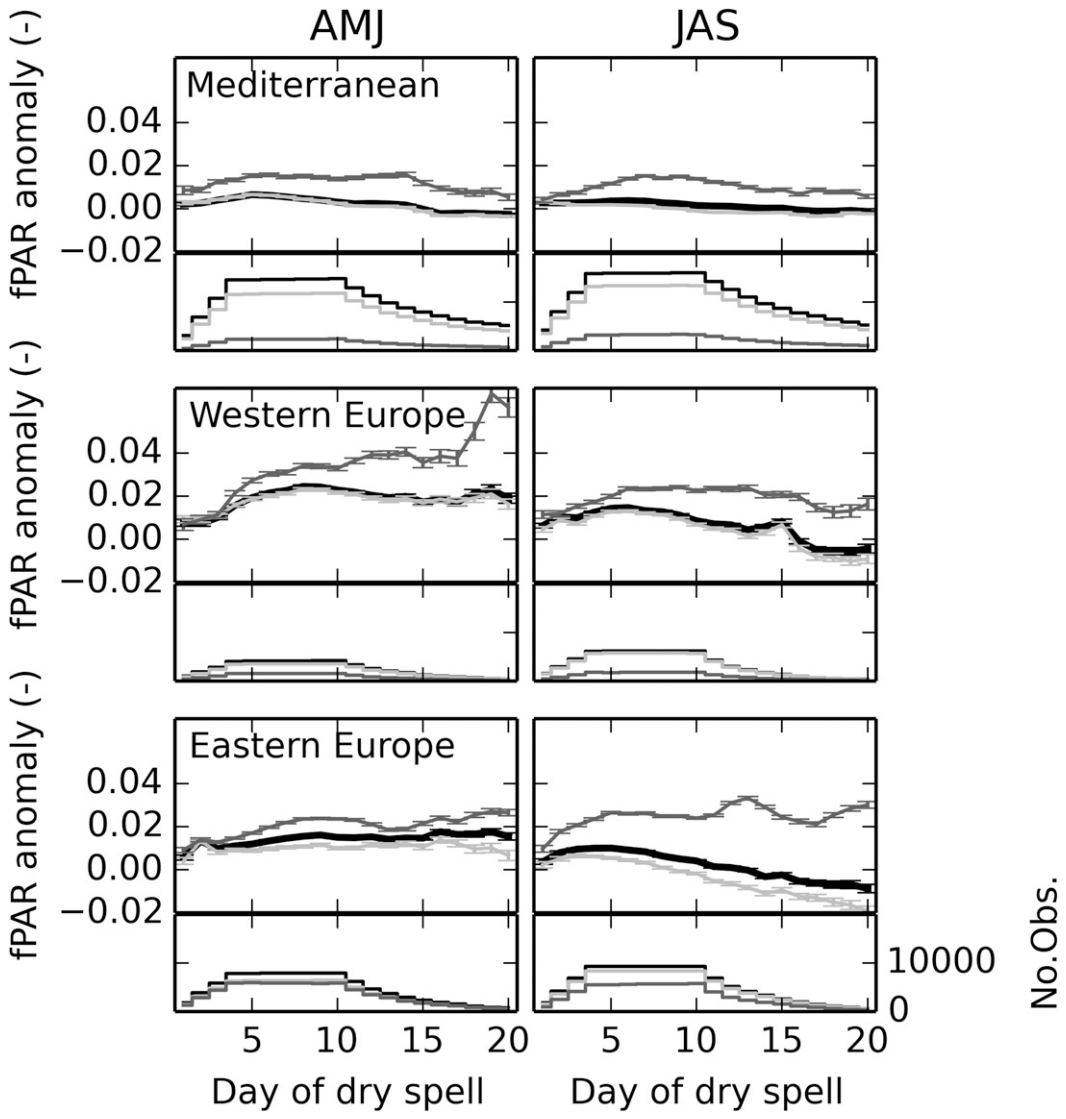

FIG. 11. Composite fPAR anomalies during dry spells for (left) spring (AMJ) and (right) late summer period (JAS), derived from 1-km pixels of all land cover (black), crop and grassland (light gray), and forest (dark gray). Step subplots indicate the number of observations on each day of the dry spell for each land-cover type. Error bars indicate standard errors on the mean.

the two dominant routes during summertime. For pixels containing a combination of vegetation and bare soil, it is not possible to separate these two sources through observations of LST alone. We expect bare soil to exhibit a stronger LST response during a dry spell than vegetation, due both to aerodynamic and hydrological effects. Here we consider changes in vegetation greenness, captured by the fraction of absorbed photosynthetically active radiation, to try to identify a purely vegetation response. Water deficits in the root zone result in a closure of the stomata in order to conserve moisture within the plant at the expense of photosynthesis, which can lead to wilting and a loss of leaf area. As previously computed using LST data, we plot the composite of fPAR anomalies for the three regions (Fig. 11), this time separated into early [April–June (AMJ)] and late summer [July–September (JAS)]. The curves are more smoothly varying over the dry spell than observed for TD, due in part to the 4-day averaging used in producing the fPAR product, but also because leaf area changes occur on much longer time scales than LST. Another consequence of the 4-day averaging is the loss of observations because of pre-onset cloud cover, leading to a slower increase in the number of observations (Fig. 11) than is seen in the daily LST. If we consider, therefore, only data from day 4 onward, we see in

all cases small positive fPAR anomalies (Fig. 11). Because of the dominance of cropland across Europe, the evolution of gridbox mean fPAR anomalies tends to follow the crop signal. For the crops, this positive anomaly early in the dry spell tends to be followed by a net decline over the second 5 days of the dry spell. The exceptions to this negative trend are in western and eastern Europe in spring. The signal over forest, however, shows positive or neutral responses to the dry spell between days 4 and 10 in all regions and both seasons. While these mean fPAR anomalies are small (particularly in the Mediterranean) and below the quoted accuracy of 0.12 RMSE for individual fPAR measurements at the 1-km scale, the data for each day within the composite are made up of typically ~10 000 separate 0.5° aggregate anomalies, each based on thousands of individual observations.

Here, we suggest possible mechanisms to explain the data in Fig. 11 as it relates to water stress on vegetation. During spring, when soil moisture deficits are small, plant growth is rapid, stimulated by warm temperatures and high radiation during dry spell episodes, particularly across central and northern Europe. By summertime, however, extended dry spells can trigger wilting or even leaf loss via root-zone soil moisture deficits, as, for example, during the 2003 heat wave (Ciais et al. 2005; Granier et al. 2007). Because forests tend to be well adapted to their environment and have access to soil moisture at depth, fPAR is less likely to decline during a dry spell than for shallow-rooted annual vegetation, at least on the time scales examined here. This is also consistent with differences in our observed surface warming rates between the two land covers (Fig. 10). For interpreting the contribution of different evapotranspiration pathways to the TD signals, it seems likely that bare soil evaporation is an important contributor, especially in the spring when seasonal vegetation growth is beginning and bare soil cover is large. As the summer progresses, we expect root-zone moisture limitations on transpiration to become increasingly important, consistent with the observed dry spell declines in fPAR. It is also worth noting the potential contamination of our signal in crop areas where harvesting occurs preferentially within dry spells.

While this study is partly motivated by the analysis of in situ flux measurements by Teuling et al. (2006), it is not possible to calculate robust estimates of *e*-folding times from our LST composites. This is primarily because of the choice of a 10-day time scale to analyze dry spells, in contrast to their analysis of longer drydown events. Our choice was driven by the need to capture many events in order to characterize the aggregate larger-scale behavior across a heterogeneous land surface. As the composites are constructed from thousands of individual dry spells, each with their own characteristic behaviors determined by local land surface properties, our approach is less useful for identifying transitions in drying behavior. On the other hand, it can tell us where in soil drying space a particular region lies, climatologically speaking. Future work will use this knowledge to evaluate land surface schemes within climate models. In this European study, stage 2 behavior is dominant. The relative importance of soil moisture for ET reflects the weighting of our observations toward the Mediterranean zone, driven by more frequent dry spells and clearer skies there. This contrasts with European flux tower–based studies such as Teuling et al. (2010), which emphasize more frequent stage 1 behavior, based on the greater availability of in situ data in more northerly locations.

7. Conclusions

Land surface temperature provides an instantaneous image of the surface energy balance integrated over different land-cover types. Here a new approach is developed, exploiting both spatial and temporal information contained within satellite LST datasets, to characterize the surface energy balance response to soil water stress. Soil moisture controls on the surface energy budget are isolated by considering dry spell events only, which are identified using an auxiliary precipitation dataset. Over Europe, dry spells are characteristic of settled weather dominated by synoptic-scale, high pressure systems that yield high numbers of clear-sky LST observations. On an event-by-event basis, the 0.5° LSTs are noisy because of a combination of subgrid sampling variability and the strong dependence of LST on local weather conditions (e.g., air temperature) on any particular day. Compositing observations over the whole domain and for all dry spell events provides on average 40 000 observations per day during the first 10–12 days and reveals a modest, yet robust, surface temperature rise on the order of 0.5–0.8 K in 10 days over and above the atmospheric warming. The rate of surface warming at any particular location depends on both land cover and initial soil moisture conditions. Consistent with a simple model of the land surface, observed dry spell warming is strongly related to rainfall accumulations in the preceding month. Over Europe the aggregate response is of increasing clear-sky sensible heat flux over the course of a 10-day dry spell, even in the aftermath of a wet month. The observations show that forests warm up more slowly than crops, an effect that is likely dominated by strong aerodynamic coupling with the atmosphere above tall vegetation. However, analysis

based on antecedent rainfall reveals that differences in hydrological behavior are also likely to be affecting the observations. Composites of the fPAR anomalies show a tendency for a positive impact on vegetation in the first few days of a dry spell, with evidence of a subsequent weak decrease in fPAR over cropland. This implies an important role in the evolution of the dry spell surface energy balance for bare soil evaporation, particularly in the spring, with transpiration effects more likely later in the dry spell.

As a consequence of employing anomalies to address subgrid sampling variabilities, comparisons of the relative warming rates over well-known surface types could lead to estimates of a gridbox-scale surface roughness that could be useful for land surface or climate models.

In this study, the number of observations on any day is limited primarily by the number of dry spell events and to some degree the definition of a dry spell imposed. The low frequency of dry spells means that only 24% of LST observations occur during a dry spell in northern France compared to 70% in southern Spain. On the other hand, 19% of the warm season dry spells identified have at least one LST observation in western Europe compared to 31% in the Mediterranean. Although the low numbers of dry spells per year in more northerly latitudes limit the applicability of the method, it is in the northern fringes of the domain that soil moisture constraints on evaporation have only a weak signal on average. Nonetheless, this analysis can be usefully applied to other regions of the world where there is high soil moisture variability, frequent clear-sky observations, and reliable atmospheric reanalyses. With careful handling of the output from GCMs to replicate the clear-sky sampling of surface temperature, it should be possible to evaluate the soil moisture sensitivity of ET in models. This opens an opportunity to potentially constrain regional projections of future climate change where that change is linked to soil hydrology (Stegehuis et al. 2013).

Acknowledgments. This research was funded under the SWELTER-21 project (NE/I006729/1) within the NERC Changing Water Cycle Programme. Additional support was provided by the European Commission's 7th Framework Programme, under Grant Agreement 282672 (EMBRACE).

REFERENCES

Anderson, M. C., J. M. Norman, J. R. Mecikalski, J. A. Otkin, and W. P. Kustas, 2007: A climatological study of evapotranspiration and moisture stress across the continental United States based on thermal remote sensing: 1. Model formulation. *J. Geophys. Res.*, **112**, D10117, doi:10.1029/2006JD007506.

——, ——, W. P. Kustas, R. Houborg, P. J. Starks, and N. Agam, 2008: A thermal-based remote sensing technique for routine mapping of land-surface carbon, water and energy fluxes from field to regional scales. *Remote Sens. Environ.*, **112**, 4227–4241, doi:10.1016/j.rse.2008.07.009.

Bastiaanssen, W. G. M., M. Menenti, R. A. Feddes, and A. A. M. Holtslag, 1998: A remote sensing surface energy balance algorithm for land (SEBAL). 1. Formulation. *J. Hydrol.*, **212–213**, 198–212, doi:10.1016/S0022-1694(98)00253-4.

Bisselink, B., E. van Meijgaard, A. J. Dolman, and R. A. M. de Jeu, 2011: Initializing a regional climate model with satellite-derived soil moisture. *J. Geophys. Res.*, **116**, D02121, doi:10.1029/2010JD014534.

Blyth, E., J. Gash, A. Lloyd, M. Pryor, G. P. Weedon, and J. Shuttleworth, 2010: Evaluating the JULES land surface model energy fluxes using FLUXNET data. *J. Hydrometeor.*, **11**, 509–519, doi:10.1175/2009JHM1183.1.

Boé, J., and L. Terray, 2008: Uncertainties in summer evapotranspiration changes over Europe and implications for regional climate change. *Geophys. Res. Lett.*, **35**, L05702, doi:10.1029/2007GL032417.

——, and ——, 2014: Land–sea contrast, soil–atmosphere and cloud–temperature interactions: Interplays and roles in future summer European climate change. *Climate Dyn.*, **42**, 683–699, doi:10.1007/s00382-013-1868-8.

Carlson, T., 2007: An overview of the "Triangle Method" for estimating surface evapotranspiration and soil moisture from satellite imagery. *Sensors*, **7**, 1612–1629, doi:10.3390/s7081612.

Castelli, F., D. Entekhabi, and E. Caporali, 1999: Estimation of surface heat flux and an index of soil moisture using adjoint-state surface energy balance. *Water Resour. Res.*, **35**, 3115–3125, doi:10.1029/1999WR900140.

Chiriaco, M., S. Bastin, P. Yiou, M. Haeffelin, J.-C. Dupont, and M. Stefanon, 2014: European heatwave in July 2006: Observations and modeling showing how local processes amplify conducive large-scale conditions. *Geophys. Res. Lett.*, **41**, 5644–5652, doi:10.1002/2014GL060205.

Christensen, J. H., and F. Boberg, 2012: Temperature dependent climate projection deficiencies in CMIP5 models. *Geophys. Res. Lett.*, **39**, L24705, doi:10.1029/2012GL053650.

Ciais, P., and Coauthors, 2005: Europe-wide reduction in primary productivity caused by the heat and drought in 2003. *Nature*, **437**, 529–533, doi:10.1038/nature03972.

Crow, W. T., W. P. Kustas, and J. H. Prueger, 2008: Monitoring root-zone soil moisture through the assimilation of a thermal remote sensing-based soil moisture proxy into a water balance model. *Remote Sens. Environ.*, **112**, 1268–1281, doi:10.1016/j.rse.2006.11.033.

Dee, D. P., and Coauthors, 2011: The ERA-Interim reanalysis: Configuration and performance of the data assimilation system. *Quart. J. Roy. Meteor. Soc.*, **137**, 553–597, doi:10.1002/qj.828.

Fischer, E. M., S. I. Seneviratne, D. Lüthi, and C. Schär, 2007a: Contribution of land–atmosphere coupling to recent European summer heat waves. *Geophys. Res. Lett.*, **34**, L06707, doi:10.1029/2006GL029068.

——, ——, P. L. Vidale, D. Lüthi, and C. Schär, 2007b: Soil moisture–atmosphere interactions during the 2003 European summer heat wave. *J. Climate*, **20**, 5081–5099, doi:10.1175/JCLI4288.1.

Garcia-Herrera, R., J. Diaz, R. M. Trigo, J. Luterbacher, and E. M. Fischer, 2010: A review of the European summer heat wave of 2003. *Crit. Rev. Environ. Sci. Technol.*, **40**, 267–306, doi:10.1080/10643380802238137.

Granier, A., and Coauthors, 2007: Evidence for soil water control on carbon and water dynamics in European forests during the extremely dry year: 2003. *Agric. For. Meteor.*, **143**, 123–145, doi:10.1016/j.agrformet.2006.12.004.

Haylock, M. R., N. Hofstra, A. M. G. Klein Tank, E. J. Klok, P. D. Jones, and M. New, 2008: A European daily high-resolution gridded data set of surface temperature and precipitation for 1950–2006. *J. Geophys. Res.*, **113**, D20119, doi:10.1029/2008JD010201.

Jung, M., and Coauthors, 2011: Global patterns of land–atmosphere fluxes of carbon dioxide, latent heat, and sensible heat derived from eddy covariance, satellite, and meteorological observations. *J. Geophys. Res.*, **116**, G00J07, doi:10.1029/2010JG001566.

Kalma, J. D., T. R. McVicar, and M. F. McCabe, 2008: Estimating land surface evaporation: A review of methods using remotely sensed surface temperature data. *Surv. Geophys.*, **29**, 421–469, doi:10.1007/s10712-008-9037-z.

Miralles, D. G., T. R. H. Holmes, R. A. M. De Jeu, J. H. Gash, A. G. C. A. Meesters, and A. J. Dolman, 2011: Global land-surface evaporation estimated from satellite-based observations. *Hydrol. Earth Syst. Sci.*, **15**, 453–469, doi:10.5194/hess-15-453-2011.

——, A. J. Teuling, C. C. van Heerwaarden, and J. V. G. de Arellano, 2014: Mega-heatwave temperatures due to combined soil desiccation and atmospheric heat accumulation. *Nat. Geosci.*, **7**, 345–349, doi:10.1038/ngeo2141.

Monteith, J. L., 1965: Evaporation and environment. *19th Symposia of the Society for Experimental Biology*, Cambridge University Press, 205–234.

Mueller, B., and Coauthors, 2011: Evaluation of global observations-based evapotranspiration datasets and IPCC AR4 simulations. *Geophys. Res. Lett.*, **38**, L06402, doi:10.1029/2010GL046230.

Norman, J. M., W. P. Kustas, and K. S. Humes, 1995: Source approach for estimating soil and vegetation energy fluxes in observations of directional radiometric surface temperature. *Agric. For. Meteor.*, **77**, 263–293, doi:10.1016/0168-1923(95)02265-Y; Corrigendum, **80**, 297, doi:10.1016/0168-1923(96)02344-1.

Peel, M. C., B. L. Finlayson, and T. A. McMahon, 2007: Updated world map of the Köppen–Geiger climate classification. *Hydrol. Earth Syst. Sci.*, **11**, 1633–1644, doi:10.5194/hess-11-1633-2007.

Quesada, B., R. Vautard, P. Yiou, M. Hirschi, and S. I. Seneviratne, 2012: Asymmetric European summer heat predictability from wet and dry southern winters and springs. *Nat. Climate Change*, **2**, 736–741, doi:10.1038/nclimate1536.

Salvucci, G. D., 1997: Soil and moisture independent estimation of stage-two evaporation from potential evaporation and albedo or surface temperature. *Water Resour. Res.*, **33**, 111–122, doi:10.1029/96WR02858.

Stap, L. B., B. J. J. M. van den Hurk, C. C. van Heerwaarden, and R. A. J. Neggers, 2014: Modeled contrast in the response of the surface energy balance to heat waves for forest and grassland. *J. Hydrometeor.*, **15**, 973–989, doi:10.1175/JHM-D-13-029.1.

Stegehuis, A. I., A. J. Teuling, P. Ciais, R. Vautard, and M. Jung, 2013: Future European temperature change uncertainties reduced by using land heat flux observations. *Geophys. Res. Lett.*, **40**, 2242–2245, doi:10.1002/grl.50404.

Tan, K. C., H. S. Lim, M. Z. MatJafri, and K. Abdullah, 2012: A comparison of radiometric correction techniques in the evaluation of the relationship between LST and NDVI in Landsat imagery. *Environ. Monit. Assess.*, **184**, 3813–3829, doi:10.1007/s10661-011-2226-0.

Teuling, A. J., and Coauthors, 2009: A regional perspective on trends in continental evaporation. *Geophys. Res. Lett.*, **36**, L02404, doi:10.1029/2008GL036584.

——, and Coauthors, 2010: Contrasting response of European forest and grassland energy exchange to heatwaves. *Nat. Geosci.*, **3**, 722–727, doi:10.1038/ngeo950.

——, S. I. Seneviratne, C. Williams, and P. A. Troch, 2006: Observed timescales of evapotranspiration response to soil moisture. *Geophys. Res. Lett.*, **33**, L23403, doi:10.1029/2006GL028178.

Vautard, R., M. Beekmann, J. Desplat, A. Hodzic, and S. Morel, 2007a: Air quality in Europe during the summer of 2003 as a prototype of air quality in a warmer climate. *C. R. Geosci.*, **339**, 747–763, doi:10.1016/j.crte.2007.08.003.

——, and Coauthors, 2007b: Summertime European heat and drought waves induced by wintertime Mediterranean rainfall deficit. *Geophys. Res. Lett.*, **34**, L07711, doi:10.1029/2006GL028001.

——, and Coauthors, 2013: The simulation of European heat waves from an ensemble of regional climate models within the EURO-CORDEX project. *Climate Dyn.*, **41**, 2555–2575, doi:10.1007/s00382-013-1714-z.

Wan, Z., 2008: New refinements and validation of the MODIS Land-Surface Temperature/Emissivity products. *Remote Sens. Environ.*, **112**, 59–74, doi:10.1016/j.rse.2006.06.026.

Weedon, G. P., G. Balsamo, N. Bellouin, S. Gomes, M. J. Best, and P. Viterbo, 2014: The WFDEI meteorological forcing data set: WATCH forcing data methodology applied to ERA-Interim reanalysis data. *Water Resour. Res.*, **50**, 7505–7514, doi:10.1002/2014WR015638.

Weisheimer, A., F. J. Doblas-Reyes, T. Jung, and T. N. Palmer, 2011: On the predictability of the extreme summer 2003 over Europe. *Geophys. Res. Lett.*, **38**, L05704, doi:10.1029/2010GL046455.

Zaitchik, B. F., A. K. Macalady, L. R. Bonneau, and R. B. Smith, 2006: Europe's 2003 heat wave: A satellite view of impacts and land-atmosphere feedbacks. *Int. J. Climatol.*, **26**, 743–769, doi:10.1002/joc.1280.

Zampieri, M., F. D'Andrea, R. Vautard, P. Ciais, N. de Noblet-Ducoudre, and P. Yiou, 2009: Hot European summers and the role of soil moisture in the propagation of Mediterranean drought. *J. Climate*, **22**, 4747–4758, doi:10.1175/2009JCLI2568.1.